ChemElectroChem

Supporting Information

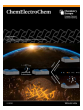

Stable and Active Oxygen Reduction Catalysts with Reduced Noble Metal Loadings through Potential Triggered Support Passivation

Daniel Göhl,* Holger Rueß, Stefanie Schlicht, Alexandra Vogel, Michael Rohwerder, Karl J. J. Mayrhofer, Julien Bachmann, Yuriy Román-Leshkov, Jochen M. Schneider, and Marc Ledendecker*

Supporting Information

1. Experimental

1.1. Synthesis and characterization of sputtered TiC film

The 510 ± 10 nm thick $TiC_{1.43\pm0.15}$ thin film was deposited in a laboratory-scale sputtering chamber by direct current magnetron sputtering (DCMS). The base pressure was below 4 x 10^{-6} mbar and the Ar deposition pressure was 1 Pa. A polished single-crystalline Al_2O_3 (001) substrate was arranged 10 cm away from the targets and was heated to 700 °C during deposition. A Ti target (power density 2.7 W/cm²) with an inclination angle of 45° with respect to the substrate normal and a C target (power density 9.9 W/cm²) facing the substrate directly were sputtered for 90 minutes, resulting in the above described thickness and composition variations.

The chemical composition of the thin films was determined by energy dispersive X-ray analysis (EDX) in a JEOL JSM-6480 scanning electron microscope (SEM) equipped with an EDAX Genesis 2000 system. X-ray diffraction (XRD) was used to study the structure using a Bruker AXS D8 Discover XRD equipped with a General Area Diffraction System (GADDS). The diffractometer was operated at a current of 40 mA and a voltage of 30 kV with Co Kα radiation at a fixed incident angle of 15°. The film thickness was determined on a Zeiss LEO 1550 VP scanning electron microscope (SEM). The wafer was mounted on the sample holder with a conductive copper tape.

Due to the Ti-C thin film synthesis approach utilizing two elemental targets, the sample exhibits a compositional range of $TiC_{0.94}$ to $TiC_{1.97}$ over 2 inches. Owing to the necessity of four different Pt depositions on top of this sample and an area resolution of the utilized electrochemical characterizations of up to 0.4 cm², a compositional range of $TiC_{1.43\pm0.15}$, which was sufficient for all measurements, was chosen. Based on X-ray diffraction (see Figure S1) and electrochemical flow cell measurements (Figure 2), no significant differences concerning the phase formation and electrochemical properties could be identified in the $TiC_{1.43\pm0.15}$ composition range.

1.2. Deposition of Pt on TiC

Pt was deposit from trimethyl(methylcyclopentadienyl)platinum ($MeCpPtMe_3$) and ozone using a commercial Gemstar-6 ALD reactor from Arradiance. The Pt-precursor was heated to 50°C, whereas the chamber temperature was set to 220°C. Ozone was produced from dioxygen in an ozone generator model BMT 803N.

Various Pt ALD cycles between 3 and 20 cycles were applied. The ALD process used was reported to exhibit a growth rate of 0.6-0.7 Å/cycle, so that the nominal thicknesses cover a

range of 2.1 to 14 Å which corresponds to 1-6 monolayers.[1,2] In the following, the nomenclature Pt_{XML}/TiC is used for the abbreviation of grown Pt on TiC where X indicates the number of deposited monolayers. The Pt-film thickness was determined by XPS measurements according to Jablonski and confirmed the assumed growth rate for the ALD process.[3,4]

1.3. Scanning kelvin probe force microscopy

Scanning kelvin probe force microscopy was conducted on a Keysight Technologies 9500 Scanning Probe Microscope. The measurements were carried out in dry air at room temperature for 7h until a stable image was obtained. The cantilever was a KS-ARROW-UHFAuD Quick Scan Nose Cone made from monolithic Si with a gold reflex coating on the detector side for electrical conduction. In the applied Kelvin Force Microscopy (KFM) mode topography of the sample and the Volta potential differences are simultaneously measured.

1.4. X-ray photoelectron spectroscopy

The surface composition of TiC before and after Pt deposition was determined on a Quantera II (Physical Electronics, *Chanhassen, MN, USA*), applying a monochromatic Al Kα X-ray source (1486.6 eV) operating at 15 kV and 25 W. The C1s signal at 285.0 eV was used to reference the binding energy scale. Analysis of the spectra has been carried out with the Casa XPS software. The homogeneity of the film was investigated by angle dependent XPS at angles of 10, 25, 45, 60, 75 and 90°. The film thickness d was calculated by Eq. (S1), whereas λ is the inelastic mean free electron path, which is assumed to be equal in Pt and TiC.[3,4] α is the angle between incident beam and analyzer, and I and I^o are the intensities of Pt and TiC in the sample and a pure reference sample.

$$d = \lambda * \cos(\alpha) * \ln\left(\frac{I_{Pt} * I^o_{TiC}}{I^o_{Pt} * I_{TiC}} + 1\right) \quad \text{(S1)}$$

1.5. Electrochemical characterization

1.5.1. Flow-cell measurements

The electrochemical measurements were conducted on the FC-ICP-MS setup, which is described in detail elsewhere.[5] Here, the sputtered Ti-C gradient films on a sapphire substrate before and after Pt deposition was used as working electrode. The electrical contact to the working electrode was ensured via a small steel needle. The geometric electrode area was determined by the opening of the FC to be 0.011 cm^2. The real electrode surface area was assumed to be identical for the sputtered films and a roughness factor of one was assumed. All currents and dissolution rates were normalized to the surface area. A

commercial Ag/AgCl (3 M KCl, *Metrohm AG, Switzerland*) electrode, placed after the outlet to the SFC, served as reference electrode. Prior to each measurement, the potential vs RHE was determined by means of a polished Pt foil to be at +0.264 V (±1 mV). All potentials herein are stated vs RHE. The counter electrode was a graphite rod placed before the inlet. A 0.1 M $HClO_4$ solution was used as electrolyte which was prepared by mixing concentrated perchloric acid (*Merck, Germany*, Suprapur®, 70%) with ultrapure water. The electrolyte was stored in a small reservoir that can be purged with different gases. From this reservoir, it was pumped with a peristaltic ICP-MS pump at constant flow rate of 188 µL/min through the SFC. For all measurements, the electrolyte was purged with Ar. After the electrolyte left the SFC, it was mixed via a V-connector with an internal standard solution containing 10 µg/L of Re. Afterwards, the electrolyte was introduced to the ICP-MS (*NexION 350X, Perkin Elmer, USA*). The ^{45}Sc, ^{48}Ti, ^{184}W and ^{187}Re isotopes were measured to monitor the concentration in the electrolyte.

Potential cycling

To establish a detailed correlation between applied potential and dissolution in the fuel cell relevant potential region, a slow CV was conducted with a scan rate of 3 mV/s from -0.2 V to +1.5 V or 0.0 to 1.5 V in case of Pt containing samples. The upper vertex potential was chosen, because during start-up and shut-down of a fuel cell, potentials as high as 1.4 to 1.5 V can arise. The delay time between onset of dissolution at the working electrode and detection at the ICP-MS detector was 17 s, which was compensated by calibrating the time scale. The peak dissolution has, however, a further uncompensated delay of 10-15 s because of the plug-flow-type concentration profile. Therefore, the resolution of the potential determinations is 30-45 mV at a scan rate of 3 mV/s.

Steady-state experiments

During fuel cell operation not the potential but the current is controlled. Therefore, the dissolution of WC at constant reduction and oxidation currents was investigated. Firstly, three reduction cycles were carried out in which an OCP period of 3 min was followed by a reduction with a current density of -0.1 mA/cm^2 over 3 min. Secondly, two oxidation cycles were conducted which were the same as the reduction cycles except that a positive current density of 0.1 mA/cm^2 was applied.

Loading determination

The loading of the ALD thin film samples was determined electrochemically by dissolving the total Pt loading on the spot enclosed by the SFC opening. Therefore, diluted aqua regia (1:20 in ultra-pure water) was used as electrolyte to increase the Pt dissolution by forming soluble

Pt complexes.[6] Due to the transient dissolution behavior of Pt, the following electrochemical procedure was carried out: First, 1500 switches between 0 and 1.5 V_{RHE} with a speed of 0.01 s $switch^{-1}$ were carried out. This led to the dissolution of Pt until the underlying TiC is passivated. In the second step, the upper potential was raised to 2.5 V_{RHE} to break the TiO_2 passivation layer by the formation of soluble TiO_2^{2+} cations.[7] The second step was repeated until Pt dissolution ceased. The first step is necessary to deactivate the Pt film as at the high potentials of step 2 oxygen evolution may occur which can cause loss of electrical contact.

1.5.2. Activity determination by RDE

The measurements were performed at room temperature on a Gamry Reference 600 potentiostat with an in-house RDE setup. A three-compartment Teflon cell was used with a graphite rod counter electrode and an Ag/AgCl reference electrode (Metrohm, 3 M KCl) which was calibrated against a reversible hydrogen electrode (RHE) at the beginning of each measurement. All potentials are reported versus RHE. The reference electrode was separated by a Nafion® membrane (Tschurl modification) to avoid chloride contamination. 0.1 M $HClO_4$ electrolyte was prepared from ultrapure water and 70% $HClO_4$. The working electrode was a 5 mm glassy carbon disk (GC). As the coated Si wafers are non-conducting at the backside, electrical contact between the carbidic front side and the GC has to be ensured. The method is explained in detail elsewhere.[8] In short, a conducting copper tape was sandwiched between the wafer and the GC, whereas the tape was long enough to fold one end onto the carbidic front side. Everything was then covered with a Kapton foil (*Ted Pella Inc., USA*) except a sample area of around 2.5 mm in diameter.

Prior to measurements, the iR drop in the cell was determined by high frequency impedance. The measurement consisted of 1) an activation protocol consisting of 200 cycles between 0.05 to 1.4 V at 200 mV/s in in Ar-sat 0.1 M $HClO_4$. 2) The ORR activity was determined in O_2-sat electrolyte conducting cycles between 0.05 and 1.2 V at 50 mV/s and rotation speeds of 400, 900, 1600 and 2500 rpm. A CV in Ar-sat electrolyte served as background. The specific and mass activity was determined from the CV recorded at 1600 rpm at 0.9 V for the anodic scan direction after the background was subtracted. The specific activity (SA) was obtained by correlating the kinetic current with the ECSA. The electrochemical active surface area (ECSA) was determined from CO-stripping and H_{UPD}, where the CV recorded direct after CO stripping served as background for the $ECSA_{CO}$ and vice versa. Conversion factors of 390 and 195 $\mu C \cdot cm^{-2}_{Pt}$, respectively, were used for CO stripping and H_{UPD} according to ref.[9] The ECSA determined via CO-stripping is a factor of 1.7 higher compared to H_{UPD} as observed for Pt(111) and PtNi(111) surfaces (Table S1).[10] The reason for that might be hydrogen spillover.[11] In such cases, van der Fliet *et al.* suggest the usage of CO stripping based ECSA. However, as the Ar background is obviously too low in the CO oxidation

region, the SA was averaged over both ECSAs (Figure S3b). This should counterbalance the overestimated $ECSA_{CO}$ and the underestimated $ECSA_{HUPD}$. The MA was determined by correlating the kinetic current with the deposited Pt amount calculated via the film thickness determined by XPS.

2. Calculations

2.1. Dissolved monolayer calculation

The amount for one dissolved monolayer of transition metal was estimated from preferentially formed surface planes. These are according to the XRD patterns the (1 1 1) and the (2 0 0) planes. Assuming that both planes are present in a 1:1 ratio (which would result in cuboctahedron), the overall surface area can be described as in Eq. (S2), where a is the fcc lattice constant of the transition metal.

$$\frac{1}{2} * A(1\,1\,1) + \frac{1}{2} * A(2\,0\,0) = \frac{\sqrt{3}}{4} * a^2 + \frac{1}{2} * a^2 = \frac{a^2}{4}\left(\sqrt{3+2}\right) \tag{S2}$$

As in each of the two planes 2 transition metal atoms are present, the number of moles per unit surface area n_{SA} can be calculated according to Eq. (S3), where N_A is Avogrado's constant.

$$n_{SA} = \frac{n}{A} = \frac{N}{A * N_A} = \frac{2}{\frac{a^2}{4}\left(\sqrt{3+2}\right) * 6{,}022 * 10^{23}\,\frac{1}{mol}} = \frac{8\,mol}{a^2\left(\sqrt{3+2}\right) * 6{,}022 * 10^{23}} \tag{S3}$$

By multiplying with the atomic weight of the transition metal M_A and the electrode surface area S_E we obtain the amount for one monolayer m_{ML} Eq. (S4)

$$m_{ML} = n_{SA} * M_A * S_E \tag{S4}$$

2.2. Dissolution efficiency

The dissolution efficiency DE is the ratio of faradaic current used for oxidizing TiC to products which are subsequently dissolved, Q_{Diss}, and the total recorded faradaic current Q_{EC} [eq. (S5)]. Q_{Diss} is calculated by Eq. (S6) and (S7). Z are the amounts of electrons involved in the oxidation, m_{Diss} is the amount of dissolved Ti measured by SFC-ICP-MS, n_{Diss} is the corresponding molar amount of TiC and F is Faraday's constant (96485 C/mol). It shall be noted that also partial oxidation to CO and Ti^{3+} can occur which would result in a lower dissolution efficiency than calculated by eq. 7.[12]

$$DE = \frac{Q_{Diss}}{Q_{EC}} \quad \text{(S5)}$$

$$TiC + 5H_2O \rightarrow TiO_2 \cdot H_2O + CO_2 + 8H^+ + 8e^- \quad \text{(S6)}$$

$$Q_{Diss} = z * n_{Diss} * F = 8 * \frac{m_{Diss}}{M_A} * F \quad \text{(S7)}$$

2.3. Expected degradation of the impaired surface

The surface of the sample was scratched with a diamond cutting tool and the surface area of the scratch was analyzed with an optical microscope. Based on the different dissolution amounts of bare TiC and protected Pt_{6ML}/TiC, the expected higher dissolution amount of the impaired surface, $f_{Scratch}$, in case of inefficient passivation can be calculated by eq. S8. Here, f_{FC} is the ratio of the surface area of the scratch $A_{Scratch}$ and the opening of the FC A_{FC}, f_{Diss} is the ratio of the amount of dissolution for bare TiC m^{TiC}_{Diss} and for Pt_{6ML}/TiC m^{6ML}_{Diss}. With f_{FC}=5% and f_{Diss}=8, this results in an $f_{Scratch}$ of 40%.

$$f_{Scratch} = f_{FC} * f_{Diss} = \frac{A_{Scratch}}{A_{FC}} * \frac{m^{TiC}_{Diss}}{m^{6ML}_{Diss}} \quad \text{(S8)}$$

3. Passivation of TiC and Pt_{6ML}/TiC

TMCs of early TMs are ceramic compounds with a high covalent bonding character between the metal t_{2g} orbitals and the carbon 2p orbitals.[13] This strong bond leads to a stabilization of the compounds against electrochemical oxidation in acidic environments far above the thermodynamic oxidation potential.[14] Once the potential is raised high enough, the TMC surface is oxidized. According to Cowling and Hintermann, the oxidation of TiC leads to the formation of initially soluble TiO^{2+} cations and CO_2 or CO, with CO favored at higher overpotentials.[12]

$$TiC + 3H_2O \rightarrow TiO^{2+} + CO_2 + 8e^- + 6H^+ \quad \text{(S9a)}$$

$$TiC + 2H_2O \rightarrow TiO^{2+} + CO + 6e^- + 4H^+ \quad \text{(S9b)}$$

Because of the low solubility of TiO^{2+} (10^{-4} M at pH=1), the electrolyte near the surface becomes oversaturated at increasingly current densities and TiO_2 is formed on top of the TiC surface.

$$TiO^{2+} + 2H_2O \rightarrow TiO_2 \cdot H_2O + 2H^+ \quad \text{(S10)}$$

In 0.1 M $HClO_4$, this passivation potentials occurs around 1.2 V_{RHE}. Continues cycling between 0.4 and 1.2 V_{RHE} shows that the DE drops declines to 40% compared to 100% at 1.0 V_{RHE} (Figure S9).

For Pt nanoparticles deposited on a TiC support, the passivation of the surface can have severe catalytic stability consequences because TiO_2 is nonconductive. However, this is not the case for the proposed thin film catalyst or core-shell nanoparticles. If we consider in the first step (Schematic S1a) a completely Pt-covered TiC substrate, degradation of the system will only occur if the potential is increased above 1.05 V_{RHE} where Pt dissolution occurs.[15] The result is the exposition of the underlying substrate or core material (Schematic S1b). If the potential is held between 1.05 V_{RHE} and 1.2 V_{RHE}, dissolution of Pt and also of the TiC substrate will continue (Schematic S1c). If the potential is raised above 1.2 V_{RHE}, the exposed TiC area will passivate via TiO_2 formation and further degradation is stopped (Schematic S1d). The usage of the damaged catalyst surface for catalysis is still possible, as the backside of the thin film is still conductive and the Pt film is in contact with TiC (Schematic S1e). This is similar for core-shell nanoparticles: as long as the Pt shell is in contact with conductive (carbon) support, the whole core-shell particle is effective for catalysis (Schematic S1f).

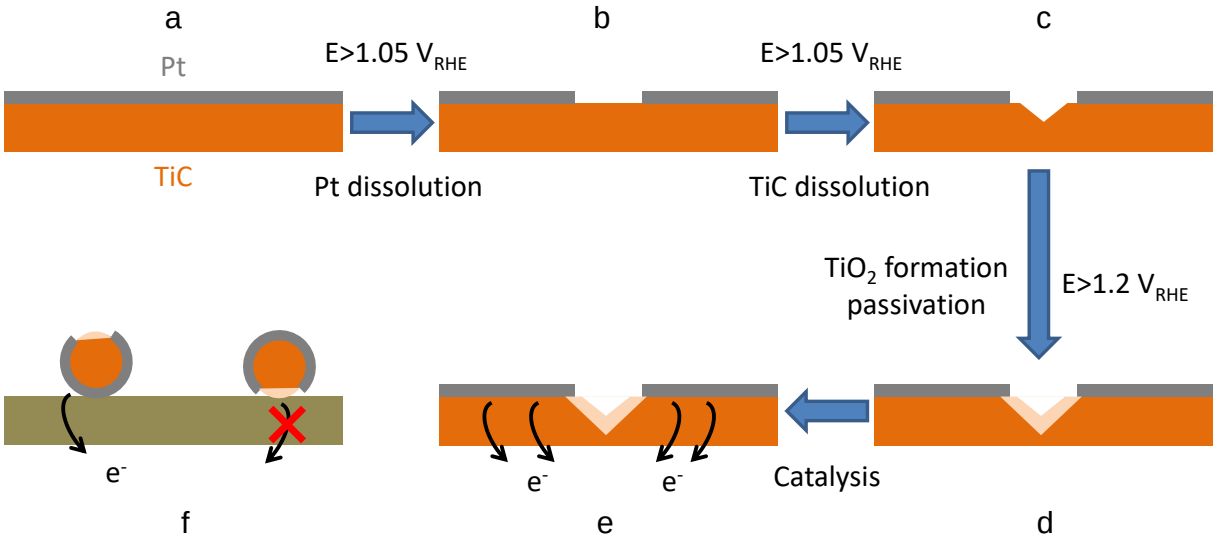

Schematic S1: Proposed passivation and stabilization mechanism of Pt_{6ML}/TiC upon a defect in the Pt shell: Upon the increase of the potential above 1.05 V_{RHE}, Pt starts to dissolve leading to the formation of a crack in the formerly homogeneous Pt film (a-b). The crack in the Pt film exposes the underlying TiC support which also dissolves at potentials above 1.05 V_{RHE} (c). If the potential is further raised above 1.2 V_{RHE}, a TiO_2 passivation layer forms on the exposed area (d). The support still covered by Pt stays intact allowing for electrical

conductivity (e). The same mechanism applies for core-shell nanoparticle if the Pt shell is in contact with the carbon support (f).

Table S1: Nominal thickness of the by ALD deposited Pt film (d_{ALD}), the thickness determined by SFC experiments (d_{SFC}) both in monolayers (ML), and the Pt mass loading on the TiC substrate.

ALD cycles	d_{ALD} [ML]	d_{SFC} [ML]	m_{Pt} [μg_{Pt} cm^{-2}]
20	6	6.9 (±0.9)	5.0 (±0.7)
10	3	1.9 (±0.4)	1.4 (±0.3)
5	1.5	0.21 (±0.05)	0.15 (±0.03)
3	1	0.12 (±0.02)	0.08 (±0.02)

Table S2: Carbon monoxide oxidation peak potentials observed during CO stripping for a bulk Pt RDE tip, 3 nm Pt nanoparticles on carbon (Pt/C) and of Pt deposited on TiC after 20 ALD cycles (Pt_{6ML}/TiC). *: The ECSA values for bulk Pt are given as roughness factor.

	$E(CO)_P$ [mV]	$ECSA_{HUPD}$ [m^2/g_{Pt}]	$ECSA_{CO}$ [m^2/g_{Pt}]	$ECSA_{CO}/ECSA_{HUPD}$
Pt bulk	761 (±15)	1.7 (±0.4)*	1.7 (±0.4)*	0.94 (±0.27)
Pt_{3ML}/TiC	795 (±7)	15(±1)	28(±6)	1.86(±0.51)
Pt_{6ML}/TiC	738 (±15)	17 (±3)	27 (±1)	1.76 (±0.13)
Pt/C	849 (±7)	70 (±17)	73 (±15)	1.03 (±0.03)

Table S3: Mean particle diameters of titanium carbide particles $d_{p,T}$ and of deposited Pt particles $d_{p,Pt}$ after 5 ALD cycles.

	$d_{p,T}$ [nm]	$d_{p,Pt}$ [nm]
TiC	120 (±20)	/
Pt_{1ML}/TiC	130 (±20)	85 (±15)
Pt_{6ML}/TiC	110 (±20)	/

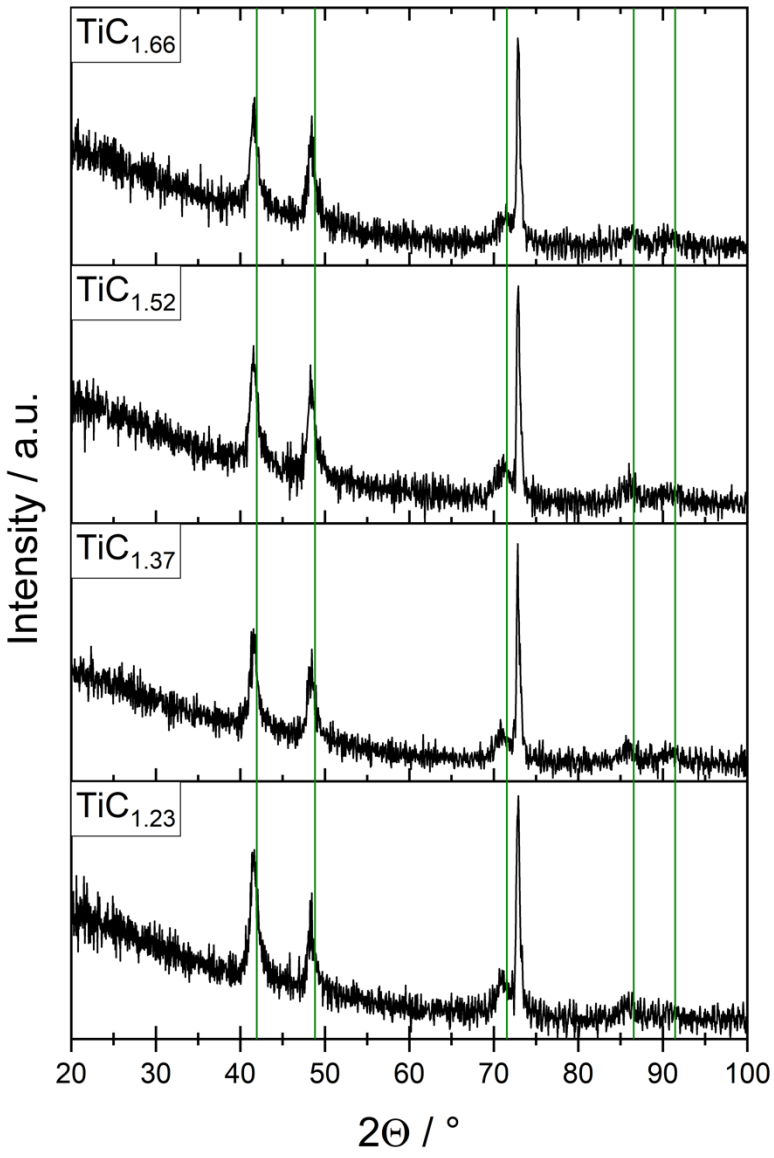

Figure S1: X-ray diffractogramms of gradient Ti-C. Reference reflexes (green lines): PDF 00-003-1213

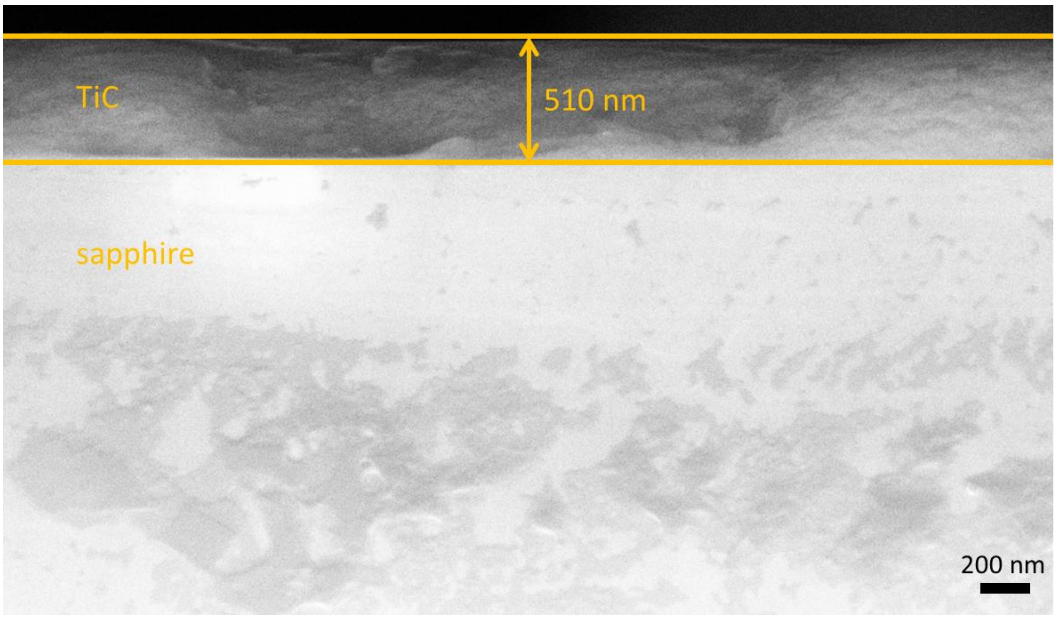

Figure S2: Cross sectional view through a TiC thin film deposited on sapphire.

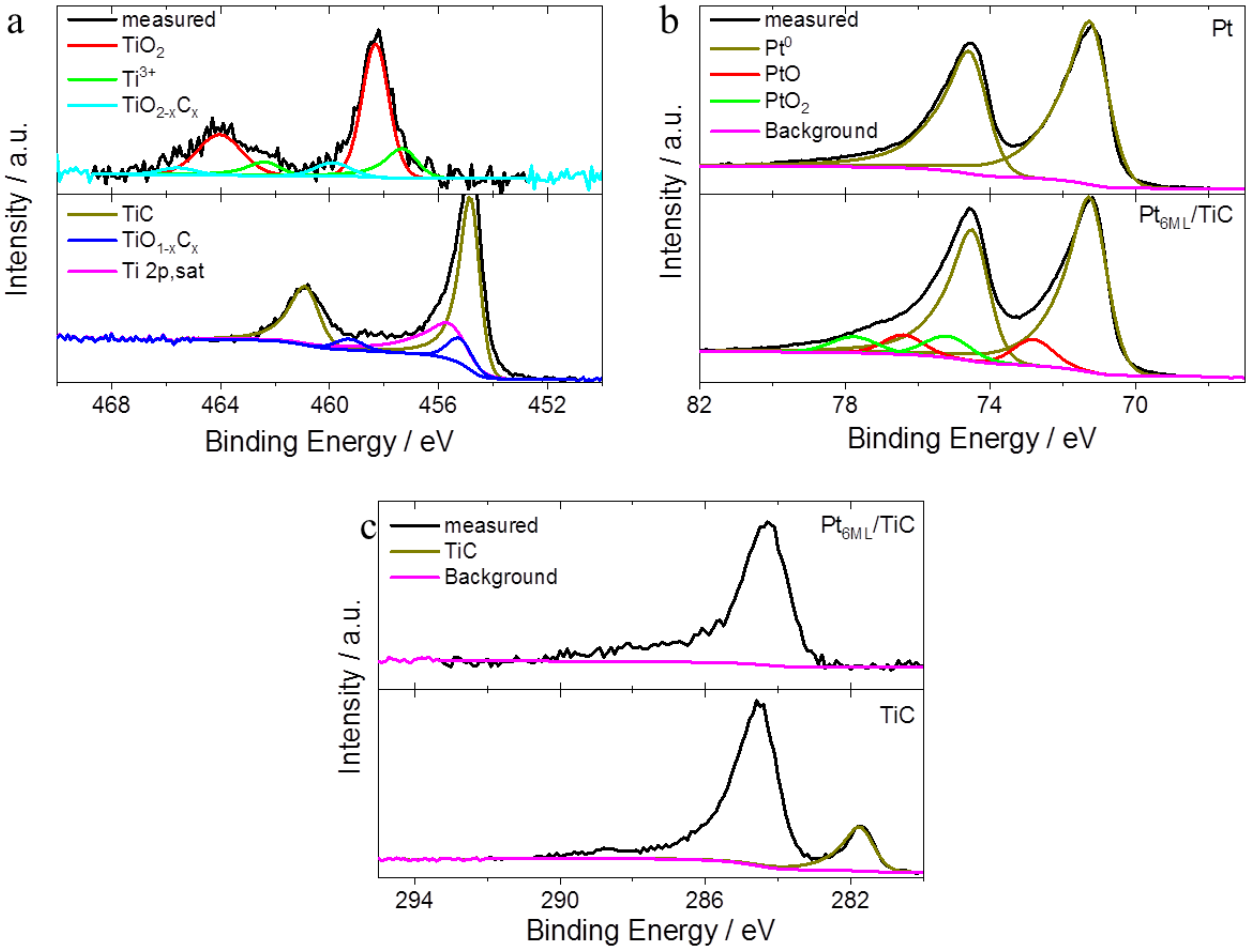

Figure S3: XPS spectrum at 45° a) of Ti 2p level measured for a pristine TiC sample and Pt_{6ML}/TiC, b) of Pt 4f level measured for a reference bulk Pt sample and Pt_{6ML}/TiC. c) of C 1s level measured for pristine TiC and of Pt_{6ML}/TiC.[16,17]

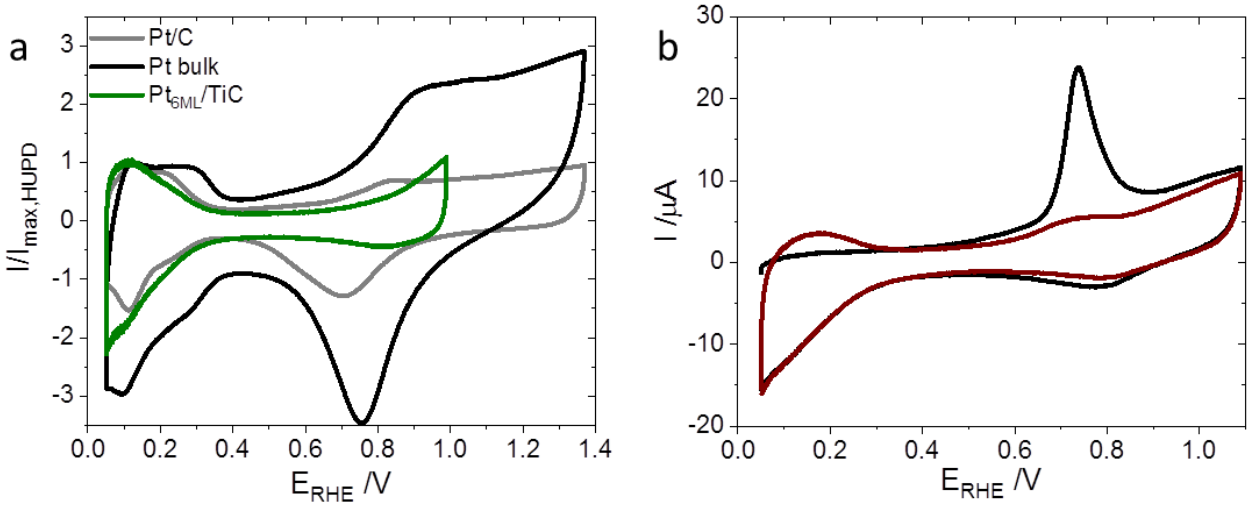

Figure S4: a) Cyclic voltammograms in Ar saturated 0.1 M $HClO_4$ at 200 mV/s of bulk Pt, 3nm Pt nanoparticles on carbon and Pt_{6ML}/TiC. For better comparison, the CVs were normalized to the maximum current observed in the anodic scan within the HUPD region. The H_{UPD} features for Pt_{6ML}/TiC are broader compared to the reference catalysts indicating a higher amount of lower coordinated Pt atoms at the surface with smaller crystalline facets compared to bulk Pt.[10] b) CO-stripping and subsequent cyclic voltammogram in Ar saturated 0.1 M $HClO_4$ at 50 mV/s of Pt_{6ML}/TiC. The baseline for CO-stripping obviously fails resulting in an overestimation of the ECSA. In contrast, hydrogen spillover from the Pt onto the TiC/TiO_x surface can result in an underestimation of the ECSA. To account for that, the ECSA values obtained by CO stripping and H_{UPD} were averaged.

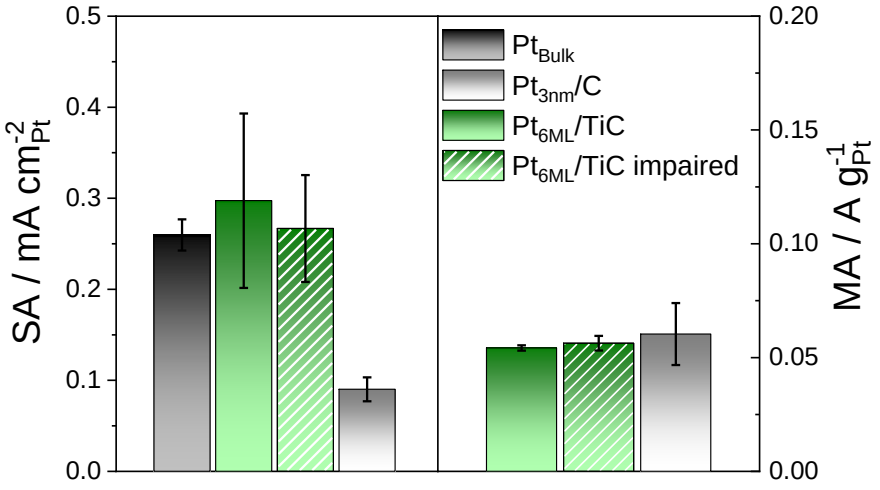

Figure S5: Oxygen reduction specific (left) and mass activities (right). The activity was determined from Koutecky-Levich's equation by subtracting the Ar-background from iR-corrected ORR polarization curves at 0.95 V_{RHE} in O_2-saturated 0.1 M $HClO_4$ at 50 mV s^{-1} and 1,600 rpm. As reference sample, 3 nm Pt nanoparticles supported on carbon (TKK, 46 wt% Pt) and a bulk Pt RDE tip were used.

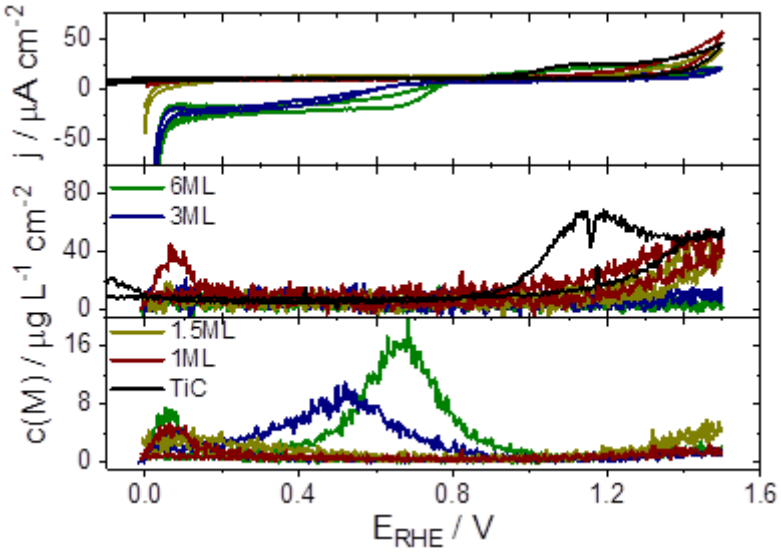

Figure S6: Cyclic voltammograms from 0.0 to 1.5 V at 3 mV s^{-1} in 0.1 M $HClO_4$ and the corresponding Ti and Pt dissolution profiles of pristine TiC, Pt_{1ML}/TiC, $Pt_{1.5ML}$/TiC, Pt_{3ML}/TiC and Pt_{6ML}/TiC.

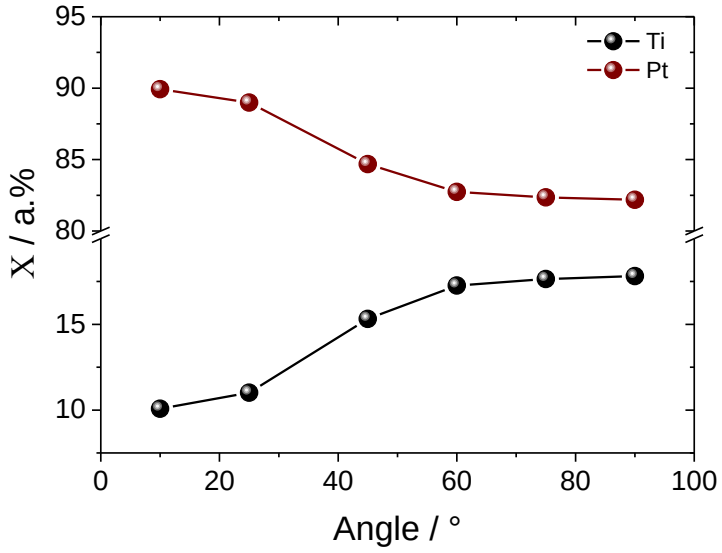

Figure S7: Measured chemical composition of Ti and Pt for Pt_{6ML}/TiC by XPS in dependence of the angle of the incident X-Ray beam. If a smooth film has been deposited, a perfect sinus like behavior of the Pt intensity and cosinus like behavior for the TiC substrate is expected.[3] Angles ranging from 90 to 10° were chosen which should ideally result in an maximum substrate attenuation of 100%*(1-cos(10°))=83%. The profile shows only a small variation in the surface composition revealing that the surface is not smooth but rough.

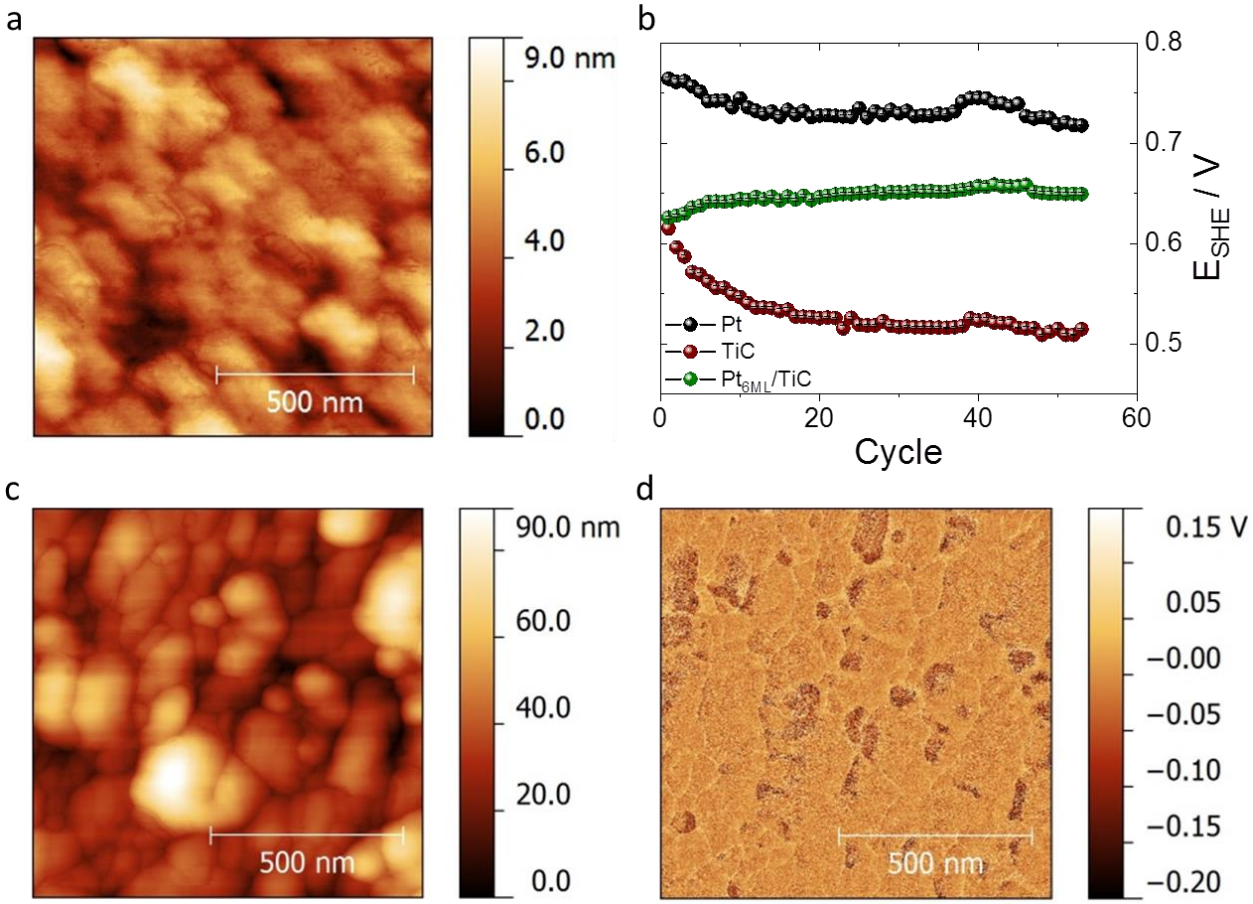

Figure S8: a) Atomic force microscopic image of a sputtered TiC surface. b) Development of the measured surface potential over 55 consecutive measurement cycles with a scanning kelvin probe under humidified air of a sputtered Pt reference, a pure TiC substrate and Pt_{6ML}/TiC. c) Topographic and d) potential scanning Kelvin probe force microscopic scans of $Pt_{1.5ML}$/TiC. The roughness is increased to 7.7 nm and supports a Volmer-Weber growth mechanism.[18]

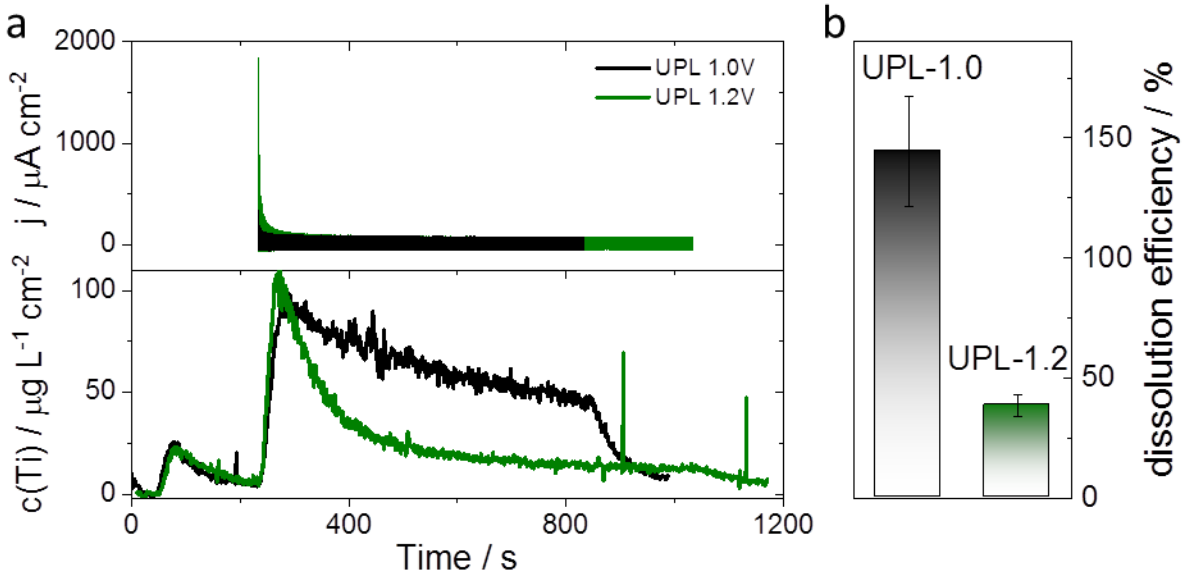

Figure S9: a) Current and Ti dissolution profile for TiC upon cycling 500 times between 0.4 and 1.0 V (UPL 1.0 V) or 1.2 V (UPL 1.2 V) at 1 V s^{-1} in 0.1 M $HClO_4$. b) Faradaic dissolution efficiency in % during for experiment a). The calculation was based on an 8 e^- process as shown in eq 1. Occurrence of incomplete oxidation to CO or Ti^{3+} can lead to the observed dissolution efficiency of over 100%.

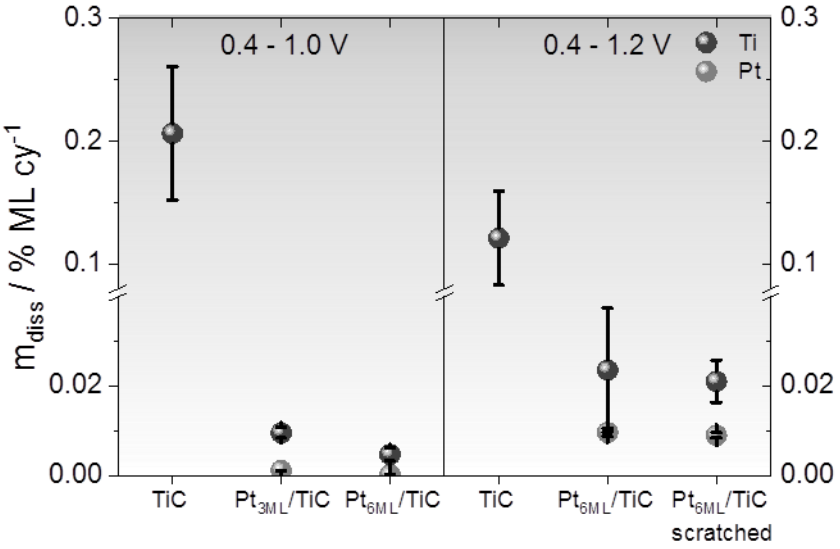

Figure S10: Total dissolution amounts per cycle during UPL 1.0 V (left) and UPL 1.2 V experiments (right) for selected samples.

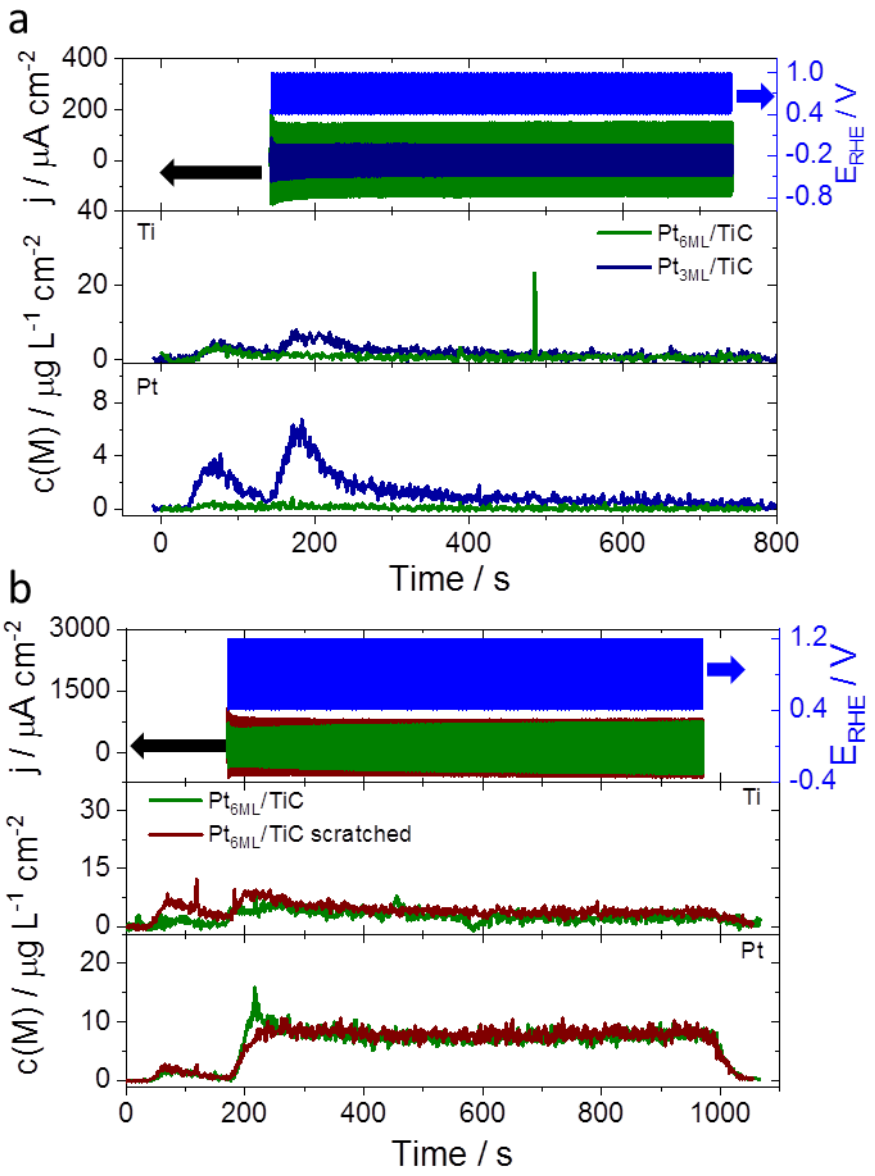

Figure S11: a) Current and Ti and Pt dissolution profile for Pt_{3ML}/TiC and Pt_{6ML}/TiC upon cycling 500 times between 0.4 and 1.0 V (UPL 1.0 V) at 1 V s^{-1} in 0.1 M $HClO_4$. b) Current and Ti and Pt dissolution profile for Pt_{6ML}/TiC with pristine and scratched surface upon cycling 500 times between 0.4 and 1.2 V (UPL 1.2 V) at 1 V s^{-1} in 0.1 M $HClO_4$.

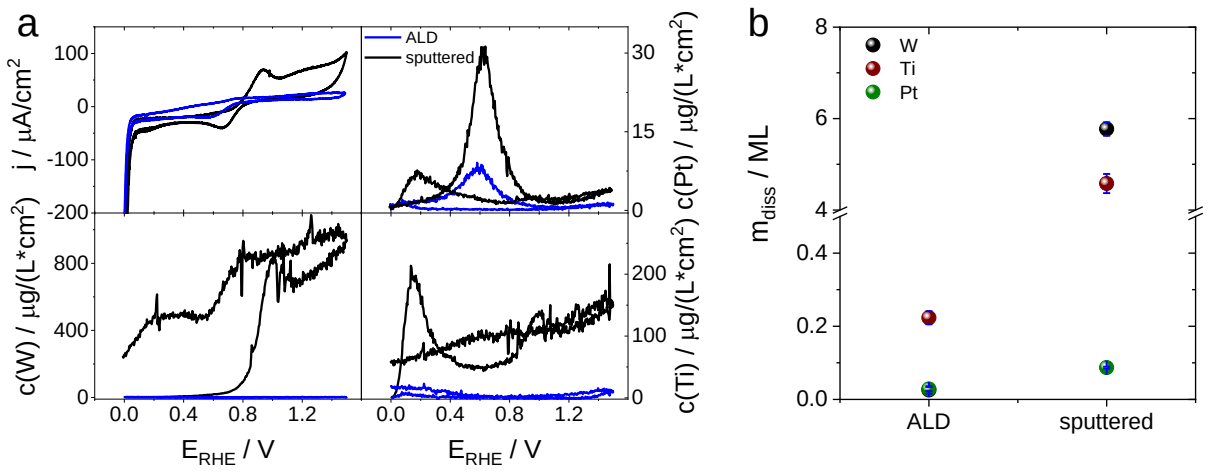

Figure S12: a) The cyclic voltammogram and the corresponding Ti, W and Pt dissolution profiles from 0.0 to 1.5 V_{RHE} at 3 mV s^{-1} in 0.1 M $HClO_4$ for sputtered and ALD deposited 5-6 ML thick Pt films on TiWC, b) the corresponding total dissolution amounts.

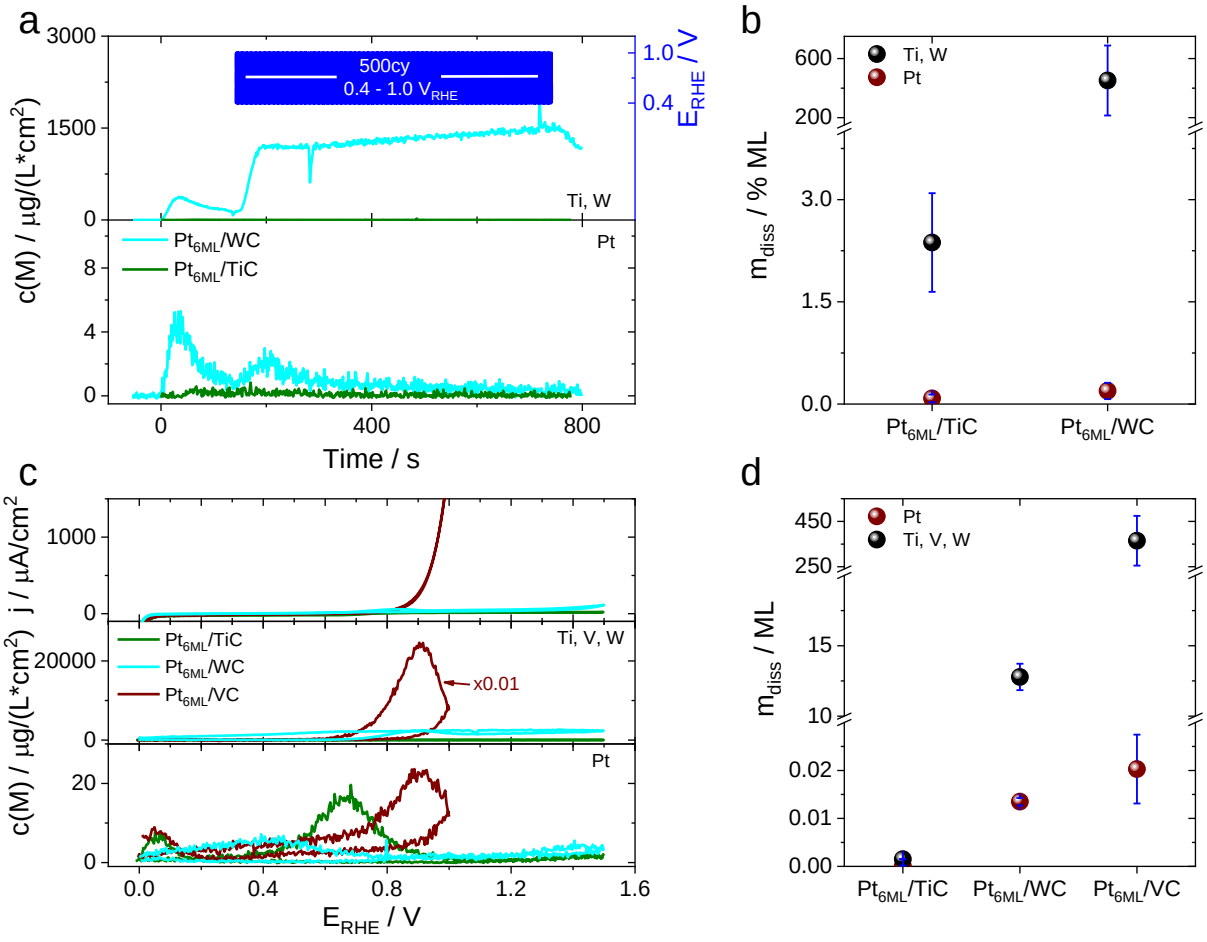

Figure S13: a) Ti and W (upper panel) and Pt (lower panel) dissolution profile for Pt_{6ML}/TiC and Pt_{6ML}/WC upon cycling 500 times between 0.4 and 1.0 V_{RHE} (UPL 1.0 V) at 1 V s^{-1} in 0.1 M $HClO_4$, b) the corresponding total dissolution amounts. c) The cyclic voltammogram and the corresponding Ti, V, W (middle panel) and Pt (lower panel) dissolution profiles from 0.0 to 1.5 V_{RHE} (1.0 V_{RHE} for VC) at 3 mV s^{-1} in 0.1 M $HClO_4$ for Pt_{6ML}/TiC, Pt_{6ML}/VC and Pt_{6ML}/WC, d) the corresponding total dissolution amounts.

References

[1] S. Schlicht, M. K. S. Barr, M. Wu, P. Hoppe, E. Spiecker, W. Peukert, J. Bachmann, *ChemElectroChem* **2018**, *5*, 3932–3937.

[2] R. Schlitz, A. A. Amusan, M. Lammel, S. Schlicht, T. Tynell, J. Bachmann, G. Woltersdorf, K. Nielsch, S. T. B. Goennenwein, A. Thomas, *Appl. Phys. Lett.* **2018**, *112*, 242403.

[3] A. Jablonski, J. Zemek, *Surf. Interface Anal.* **2009**, *41*, 193–204.

[4] C. J. Powell, A. Jablonski, *NIST Electron Inelastic-Mean-Free-Path Database, SRD*

71, National Institute Of Standards And Technology, Gaithersburg MD, **2010**.

[5] J.-P. Grote, A. R. Zeradjanin, S. Cherevko, K. J. J. Mayrhofer, *Rev. Sci. Instrum.* **2014**, *85*, 104101.

[6] S. Geiger, S. Cherevko, K. J. J. Mayrhofer, *Electrochim. Acta* **2015**, *179*, 24–31.

[7] M. Pourbaix, *Atlas of Electrochemical Equilibria in Aqueous Solutions*, NACE Interntional Ceelcor, Houston, Brussels, **1966**.

[8] M. D. Pohl, S. Haschke, D. Göhl, O. Kasian, J. Bachmann, K. J. J. Mayrhofer, I. Katsounaros, *J. Electrochem. Soc.* **2019**, *166*, H791–H794.

[9] K. J. J. Mayrhofer, D. Strmcnik, B. B. Blizanac, V. Stamenkovic, M. Arenz, N. M. Markovic, *Electrochim. Acta* **2008**, *53*, 3181–3188.

[10] D. F. Van Der Vliet, C. Wang, D. Li, A. P. Paulikas, J. Greeley, R. B. Rankin, D. Strmcnik, D. Tripkovic, N. M. Markovic, V. R. Stamenkovic, *Angew. Chem. Int. Ed.* **2012**, *51*, 3139–3142.

[11] D. V. Malevich, V. B. Drozdovich, I. M. Zharskii, *Stud. Surf. Sci. Catal.* **1997**, *112*, 359–366.

[12] R. D. Cowling, H. E. Hintermann, *J. Electrochem. Soc.* **1970**, *117*, 1447–1449.

[13] J. Häglund, A. Fernández Guillermet, G. Grimvall, M. Körling, *Phys. Rev. B* **1993**, *48*, 11685–11691.

[14] D. Göhl, H. Rueß, M. Pander, A. R. Zeradjanin, K. J. J. Mayrhofer, J. M. Schneider, A. Erbe, M. Ledendecker, *J. Electrochem. Soc.* **2020**, *167*, 21501.

[15] A. A. Topalov, I. Katsounaros, M. Auinger, S. Cherevko, J. C. Meier, S. O. Klemm, K. J. J. Mayrhofer, *Angew. Chem. Int. Ed.* **2012**, *51*, 12613–12615.

[16] A. A. Galuska, J. C. Uht, N. Marquez, *J. Vac. Sci. Technol. A Vacuum, Surfaces, Film.* **1988**, *6*, 110.

[17] H. H. Hwu, J. G. Chen, *Chem. Rev.* **2005**, *105*, 185–212.

[18] M. Volmer, A. Weber, *Zeitschrift für Phys. Chemie* **1926**, *119U*, 277–301.